Matter

CellPress
OPEN ACCESS

Article

Functionalized wood with tunable tribopolarity for efficient triboelectric nanogenerators

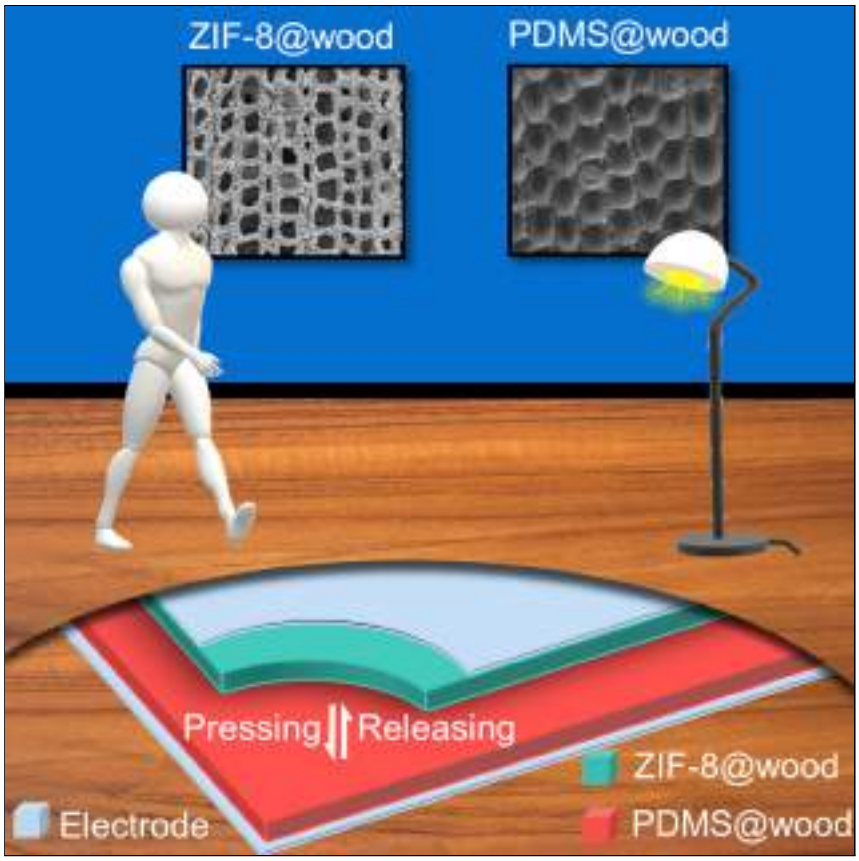

We describe a functional wood triboelectric nanogenerator (FW-TENG) made by modifying a wood scaffold respectively with ZIF-8 and PDMS. Our approach enables wood with a wide spectrum of triboelectric polarities while preserving its sustainability and aesthetic appearance. We demonstrate the application of our FW-TENG as an energy-harvesting wooden floor or panel, allowing it to power household lamps and other electronic devices when activated by walking or tapping.

Jianguo Sun, Kunkun Tu, Simon Büchele, ..., Javier Pérez-Ramírez, Ingo Burgert, Guido Panzarasa

guido.panzarasa@ifb.baug.ethz.ch

Highlights

Efficient approach to increase and tune the triboelectric polarity of native wood

Wood scaffolds are functionalized with ZIF-8 and PDMS

Wide selection of parameters allows tuning the triboelectric output

Demonstration of functional wood TENGs suitable for large-scale applications

4 **Demonstrate**
Proof-of-concept of performance with intended application/response

Sun et al., Matter 4, 3049–3066
September 1, 2021
Published by Elsevier Inc.
https://doi.org/10.1016/j.matt.2021.07.022

Matter

CellPress
OPEN ACCESS

Article

Functionalized wood with tunable tribopolarity for efficient triboelectric nanogenerators

Jianguo Sun,[1,2,7] Kunkun Tu,[1,2,7] Simon Büchele,[3] Sophie Marie Koch,[1,2] Yong Ding,[1,2] Shivaprakash N. Ramakrishna,[4] Sandro Stucki,[1,2] Hengyu Guo,[5] Changsheng Wu,[6] Tobias Keplinger,[1,2] Javier Pérez-Ramírez,[3] Ingo Burgert,[1,2] and Guido Panzarasa[1,2,8,*]

SUMMARY

Wood is a state-of-art, renewable, and sustainable building material with excellent mechanical properties but negligible triboelectric polarizability. Strategies to improve and rationally tune the triboelectric properties of wood are needed to further its application for mechanical energy harvesting in smart buildings. We found that wood becomes more triboelectrically positive when modified by *in situ*-grown zeolitic imidazolate framework-8 (ZIF-8), a metal-organic framework (MOF), and more triboelectrically negative when coated with poly(dimethylsiloxane) (PDMS). A triboelectric nanogenerator (TENG) made with two radial-cut wood samples (L × R × T: 35 × 20 × 1 mm^3), respectively functionalized with ZIF-8 and PDMS, can generate an open-circuit voltage (Voc) of 24.3 V and a short-circuit current (Isc) of 0.32 μA upon 50 N, 80 times higher compared with that of native wood. We demonstrate the applicability of our functionalized wood TENG (FW-TENG) in smart buildings by using it to power household lamps, calculators, and electrochromic windows.

INTRODUCTION

The concept of "smart building" has witnessed ever-increasing attention in recent decades. Conventional approaches heavily rely on power supplies with limited lifetime (batteries),[1–3] so that increasing environmental and technological concerns motivated the emergence of triboelectric nanogenerators (TENGs) for the direct conversion of mechanical energy (e.g., inhabitants' movements) into useful electricity.[4–7] However, typical TENGs are often made from non-sustainable highly fluorinated polymers, such as poly(tetrafluoroethylene) (PTFE), obtained from non-renewable sources and difficult to recycle, and thus inappropriate for large-scale applications in smart homes.[6,8–11]

Wood, one of the most abundant natural biomaterials on Earth, is convenient, renewable, biocompatible, biodegradable, and has been used as an excellent construction material for thousands of years.[12] For these reasons, wood would be an ideal material to be implemented in TENGs for large-scale applications in smart homes. Nevertheless, native wood has a negligible triboelectric effect due to its weak polarizability, limiting its ability to generate surface charges. In the triboelectric series, which orders materials from the most electron-donating (tribopositive) to the most electron-attracting (tribonegative), native wood nearly sits in the middle; i.e., close to electro-neutrality. This may account for the absence of significant progress in the

Progress and potential

The energy efficiency of buildings could be strongly improved by enabling building materials to convert their occupants' mechanical energy directly into useful electricity. In this regard, approaches based on triboelectric effects are especially promising. Wood is an excellent building material, highly appreciated for its intrinsic sustainability, low cost, as well as aesthetic value. However, due to its weak polarizability and poor triboelectric performance, the use of wood as a triboelectric energy source has yet to be exploited. Here, we tackled the problem of weak polarizability of native wood by functionalizing wood scaffolds with ZIF-8 and PDMS and assembling them in triboelectric nanogenerators (TENGs). Our functionalized wood TENGs (FW-TENGs) show potential as energy-harvesting floors in smart buildings.

development of wood-based TENGs so far.[6,13] Pairing materials with opposite tribo-polarities, and increasing surface roughness to facilitate contact, are effective strategies to improve the electrical performance of TENGs.[14–16] In recently proposed examples of wood-based TENGs, the triboelectric output was generated by simply coupling native wood with highly polarizable materials (such as PTFE). In such approaches, however, wood itself does not play a role in improving the output performance of TENG.[6,17] To promote the use of wood in TENGs, it is thus necessary to develop approaches to increase, and tune, the triboelectric polarizability of wood.

Metal-organic frameworks (MOFs) are porous materials composed of metal ions coordinated by organic ligands. MOFs have been identified as highly promising triboelectric materials thanks to their flexibility regarding composition, size, and functionality.[18–20] In particular, the zeolitic imidazolate framework-8 (ZIF-8), a subclass of MOFs with sodalite topology, has been shown to display positive triboelectric behavior.[18] In addition to its tribopositive behavior, the unique particle geometry and the possibility to tune its size, thus adjusting the nano-roughness of ZIF-8-functionalized triboelectric surfaces, make it a promising candidate for the development of TENGs. However, the challenging processability of its powder form limited the application of ZIF-8 use in TENGs.[21] On the other hand, poly(dimethylsiloxane) (PDMS) is an industrial polymer with excellent electron-accepting properties and good flexibility, making it an almost ideal tribonegative layer. However, there is still a long way to go for using pure PDMS to satisfy smart building applications, especially because this requires increasing its surface roughness by means of complicated and energy-consuming processes.[22–24]

Surface modification of native wood with ZIF-8 and PDMS allowed researchers to change its triboelectric properties, making it more tribopositive (ZIF-8@wood) and more tribonegative (PDMS@wood), thus enhancing the electrical output. However, changes in the surface chemical composition alone cannot be considered solely responsible for the observed behavior. As a scaffold, wood provides increased mechanical strength and toughness, and also its natural micro- and nanoscale roughness can influence the triboelectric properties of the composite. The specific roughness manifests differently due to wood's hierarchical structure, and depends both on the chosen wood species and the cutting direction. For this reason, we investigated the effects of different wood species and cutting directions, as well as of different ZIF-8 sizes, on the triboelectric output of the wood composites. The resulting optimized functional wood triboelectric nanogenerator (FW-TENG) displayed a triboelectric output over 80 times higher than that of a native wood TENG, and could be used to power household devices (from lamps to calculators) as well as to actuate a miniature electrochromic window, useful to modulate indoor lighting.[25–27] Our study will inform the design of next-generation energy-efficient building materials.

RESULTS

Our approach for the fabrication of a functionalized wood triboelectric nanogenerator (FW-TENG) is represented schematically in Figure 1A. Two pieces of wood veneer are modified, respectively, with ZIF-8 particles (by *in situ* growth) and with PDMS (by spin coating and curing). The resulting surface chemical and morphological changes increase the ability of wood to donate (ZIF-8@wood) or acquire (PDMS@wood) electrons during periodic contact-separation cycles and, consequently, the amount of electricity produced. Metal electrodes are then attached on the back side of each functionalized veneer to collect and transfer the electrostatically induced charges through an external circuit.

[1]Wood Materials Science, Institute for Building Materials, ETH Zürich, 8093 Zürich, Switzerland

[2]WoodTec Group, Cellulose & Wood Materials, Empa, 8600 Dübendorf, Switzerland

[3]Institute for Chemical and Bioengineering, Department of Chemistry and Applied Biosciences, ETH Zürich, 8093 Zürich, Switzerland

[4]Surface Science and Technology, Department of Materials, ETH Zürich, 8093 Zürich, Switzerland

[5]School of physics, Chongqing University, 400054 Chongqing, China

[6]Querrey Simpson Institute for Bioelectronics, Northwestern University, Evanston, IL 60208, USA

[7]These authors contributed equally

[8]Lead contact

*Correspondence: guido.panzarasa@ifb.baug.ethz.ch

https://doi.org/10.1016/j.matt.2021.07.022

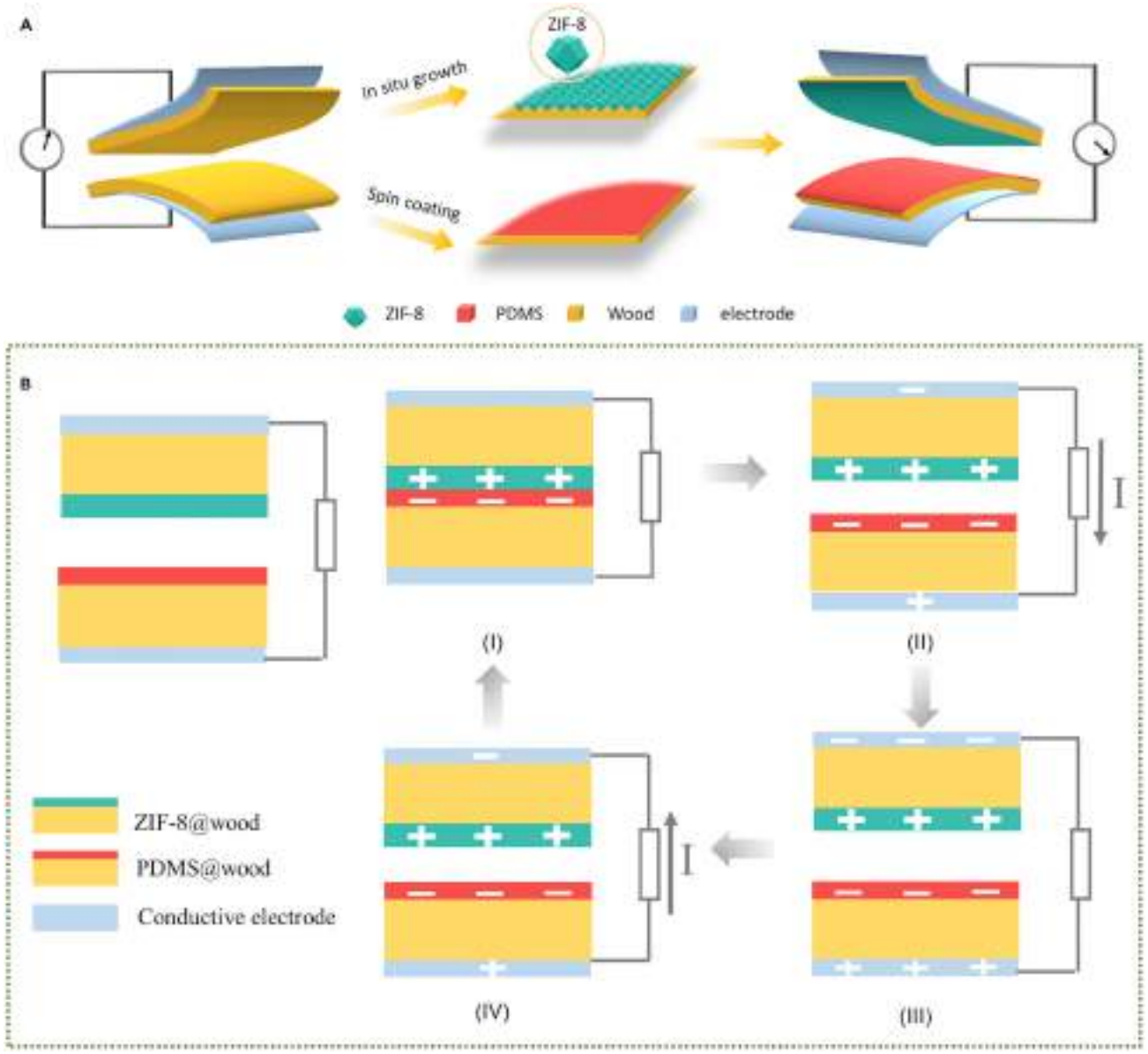

Figure 1. Schematic representation of the fabrication and working mechanism of our FW-TENG
(A) Schematic representation of the FW-TENG made with ZIF-8@wood and PDMS@wood.
(B) Schematic representation of the triboelectrification process in our FW-TENG.

The working principle of our FW-TENG is illustrated in Figure 1B, with the coupled effects of contact electrification and electrostatic induction.[2] When the more tribo-positive ZIF-8@wood is put in contact with the more tribonegative PDMS@wood, static charges of opposite sign are generated by contact electrification. Electrons transfer from the surface of ZIF-8@wood to the surface of PDMS@wood, resulting in fully balanced, electrostatically paired charges. There is no electron flow in the external circuit at this stage (stage I).[10,28] Once the two layers are separated, the negative charges on the surface of PDMS@wood cannot be compensated by the ones on the surface of ZIF-8@wood, inducing a potential difference across the top and bottom electrodes. Simultaneously, opposite charges are induced on the electrodes under the action of electrostatic induction. In order to screen this

potential difference, the electrostatically induced free charges will be driven to flow between the two conductive electrodes through the external load (stage II). Both the current and voltage outputs are generated during this process until the potentials of the two electrodes reach equilibrium again (stage III). Once the ZIF-8@wood is reverted to approach the PDMS@wood, the potential difference will begin to decrease, driving the charges to flow back in the opposite direction until the original state is attained, resulting in a reversed electrical output (stage IV).[29]

It has already been demonstrated[30,31] that the internal circuit in a TENG is determined by the displacement current (first introduced by Maxwell in 1861, it is not an electric current of moving free charges[32]), while the observed current in the external circuit is the capacitive conduction current. As shown in Figure S1, the internal circuit and external circuit meet at the two electrodes to form a loop. Therefore, the displacement current is the intrinsic physical core of current generation, while the capacitive conduction current is the external manifestation of displacement current.[31]

To investigate the effect of wood microstructure on the electrical output performance, three wood species (balsa, spruce, and yew), widely different in terms of cell structure, porosity (from 64% to 16%, Figure S2 and Table S1), and density (from 83 kg m^{-3} to 814 kg m^{-3}), were tested in the present study. Figures 2A, 2B, and S3 display the scanning electron microscopy (SEM) images of cross-cuts (C) of balsa, spruce, and yew. Balsa wood is a lightweight, diffuse-porous hardwood species, mainly composed of vessels, parenchyma cells, and fibers aligned along the longitudinal direction. It is different from spruce and yew, which are both softwoods and have relatively similar anatomical features. However, on average, yew tracheids have a lower lumen diameter and a higher cell wall thickness than spruce, which is reflected in a much higher density.[33] Different wood species thus have different surface morphologies, which in turn display different microstructures. We also investigated the influence of morphologies originating from different cutting directions. Spruce wood was cut into three planes: cross (C), radial (R), and tangential (T). As shown in Figures 2B–2D, these three cuts have different morphologies and microstructures due to the intrinsic anisotropy of wood, resulting in different surface roughness.

Nanocrystals of ZIF-8 were then grown on wood using a two-step synthesis process. First, wood was pretreated with an alkaline solution to generate nucleation sites, which promoted a stable attachment of the nanocrystals. Then, ZIF-8 nanocrystals were grown by the stepwise addition of zinc nitrate $Zn(NO_3)_2$ and 2-methylimidazole (2-MeIm) solutions. The size of ZIF-8 nanocrystals can be tuned by controlling the ratio between ligand (2-MeIm) and metal ions (Zn cations, Zn^{2+}). When the 2-MeIm/Zn^{2+} molar ratio was increased from 5 to 20, the average ZIF-8 particle size increased from ~616 nm to ~1,008 nm, and the associated particle size distribution broadened. (Figures S4 and S5). The typical morphology of a ZIF-8@wood sample, prepared with a 2-MeIm/Zn^{2+} molar ratio of 20 (20-ZIF-8@wood), is shown in Figures 2E–2H and S6. As can be seen in Figure 2E, the structure of the analogue 20-ZIF-8@balsa(C) is dramatically affected by the alkaline pretreatment, which partially removes lignin and hemicelluloses, causing the cell walls to wrinkle and resulting in extensive shrinkage after drying (Figure S7).[19] The SEM images of wood samples coated with PDMS are shown in Figures 2I–2L and S8. Compared with that of native wood, the surface of PDMS@wood is smoother. In particular, cross-cut wood samples are no longer macroporous, since the PDMS is entirely covering the whole surface as well as the lumina, forming a concave surface. The thickness of the PDMS film

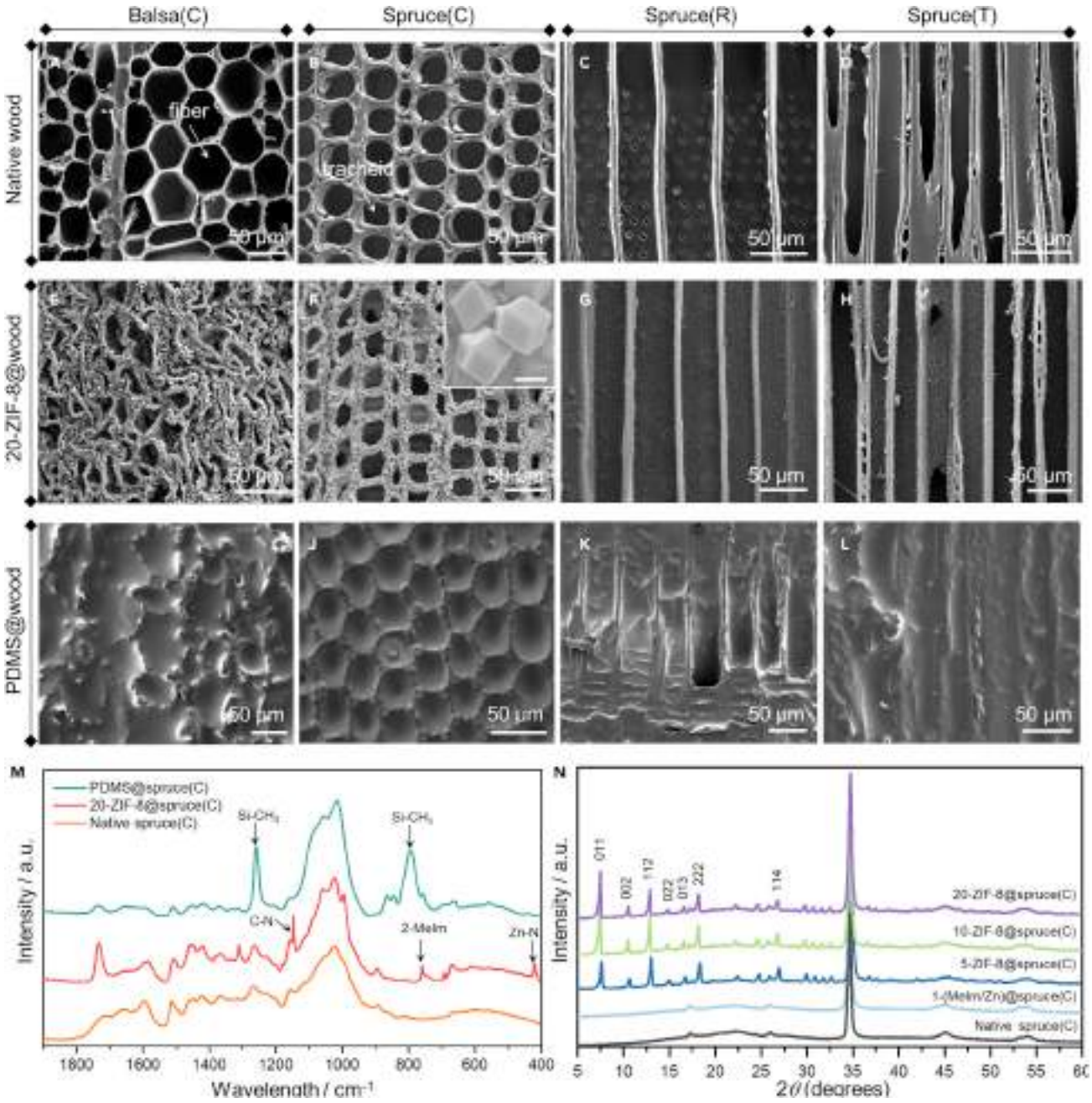

Figure 2. Morphological and physico-chemical characterization of native wood, ZIF-8@wood, and PDMS@wood samples

(A–L) (A–F) SEM images of cross-cut balsa (first column) and spruce wood (second column), radial-cut spruce (third column), and tangential-cut spruce (fourth column) (A–D) without functionalization, (E–H) after functionalization with *in situ*-grown ZIF-8 (2-MeIm/Zn^{2+} = 20), and (I–L) after functionalization with PDMS. Inset in (F) shows the morphology of ZIF-8 grown on wood (scale bar of e: 500 nm).

(M) FTIR spectra of native spruce(C), 20-ZIF-8@spruce(C), and PDMS@spruce(C), respectively.

(N) XRD results for native spruce (C) and ZIF-8@spruce(C) with an increased 2-MeIm/Zn^{2+} ratio from 5 to 10, and 20, as well as 1-(MeIm/Zn)@spruce(C), respectively. The spruce samples used here are cross-cut by laser, resulting in an unusual cellulose peak intensity distribution. For more details, Figure S11 shows the XRD spectra of different sections (tangential, radial, and cross section) of native spruce veneer prepared with different methods (saw cutting, laser cutting).

coated on different wood species is within 10 μm, much smaller than the thickness of wood (1 mm), as shown in Figure S9. These results show that the modification of wood, both with ZIF-8 and PDMS, introduces relevant morphological changes.

By functionalizing wood with PDMS and ZIF-8, the wood surface's chemical composition was changed as well (Figures 2M and 2N and S10). The Fourier transform infrared (FTIR) spectra of PDMS@spruce(C), 20-ZIF-@spruce(C), and native spruce(C) samples are displayed in Figure 2M. The strongest absorption bands for PDMS@spruce(C) are at 796 cm^{-1} (Si–C stretching in Si–CH_3) and 1,258 cm^{-1} (deformation of –CH_3 in Si–CH_3), confirming the presence of PDMS on the surface.[34] On the other hand, the 20-ZIF-8@spruce(C) sample shows bands at 1,147 cm^{-1}, 422 cm^{-1}, and 759 cm^{-1}, associated with the stretching of C–N and Zn–N bonds, and the out-of-plane bending of the 2-MeIm ring, which confirms the successful modification of wood with ZIF-8. Both the 5-ZIF-8@spruce(C) and 10-ZIF-8@spruce(C) samples have FTIR spectra similar to that of the 20-ZIF-8@spruce(C), the only notable exception being 1-ZIF-8@spruce(C) (Figure S10). This difference can be explained by taking into account the associated powder X-ray diffraction (XRD) patterns (Figure 2N). The strong peaks at 2θ = 7.48, 10.54, 12.88, 14.80, 16.58, and 18.16°, which correspond respectively to planes (011), (002), (112), (022), (013), and (222), indicate the high crystallinity of the 5-, 10-, and 20-ZIF-8 samples. However, 1-ZIF-8@spruce(C) shows only an XRD pattern similar to that of native spruce (C), without the typical peaks from ZIF-8 crystals, suggesting that a 2-MeIm/Zn^{2+} ratio of 1 does not result in ZIF-8 formation (Figures 2N and S11). The amount of Zn incorporated by each kind of sample was measured by inductively coupled plasma-optical emission spectrometry (ICP-OES) and used to calculate the percentage of MOF loading. Results (Table S2) showed that the 5-, 10-, and 20-ZIF-8@spruce(C) composites had similar ZIF-8 contents, respectively 11.0 wt %, 9.3 wt %, and 8.8 wt %, while a Zn-based material of unknown structure was generated with a 2-MeIm/Zn^{2+} ratio of 1 (sample 1-(MeIm/Zn)@spruce(C)).

Higher surface roughness usually results in an increased effective surface area, thus improving the electrical performance of a TENG.[10,35] However, an excessively rough surface can produce tip-to-tip contacts between the triboelectric materials, causing incomplete contact and consequently decreasing the electrical output.[36] Hence, control of surface roughness is vital for TENGs. Although the real contact area may be proportional to surface roughness, its quantitative analysis remains an open challenge due to the many factors that need to be taken into account (such as applied mechanical load, number of microcontacts, and conductance between the surfaces).[37,38] Therefore, a more empirical approach is conventionally adopted, in which differences in the electrical output are directly related to changes in surface morphology and roughness. Surface roughness can be increased by surface micro/nano-structuration techniques, including photolithography templates, nanoimprint, and physical/chemical etching.[39–41] However, these methods require complex processes and dedicated instrumentation. Here we take advantage of the variety of wood's microstructures to generate unique micro/nano-roughness through its functionalization with ZIF-8 nanocrystals and PDMS.

Figures 3A, 3B, and S12 show 3D surface profiling images of cross-cut native balsa, spruce, and yew, respectively. As shown in Table S3, different wood species, cut with the same directions, lead to different surface roughness. Native balsa(C) has the highest average roughness (Ra) value of 11.9 μm, while native yew(C) the lowest (6.5 μm). Figures 3C and 3D show 3D surface profiling images of tangential- and radial-cut native spruce, respectively. Compared with the Ra value of native spruce(C)

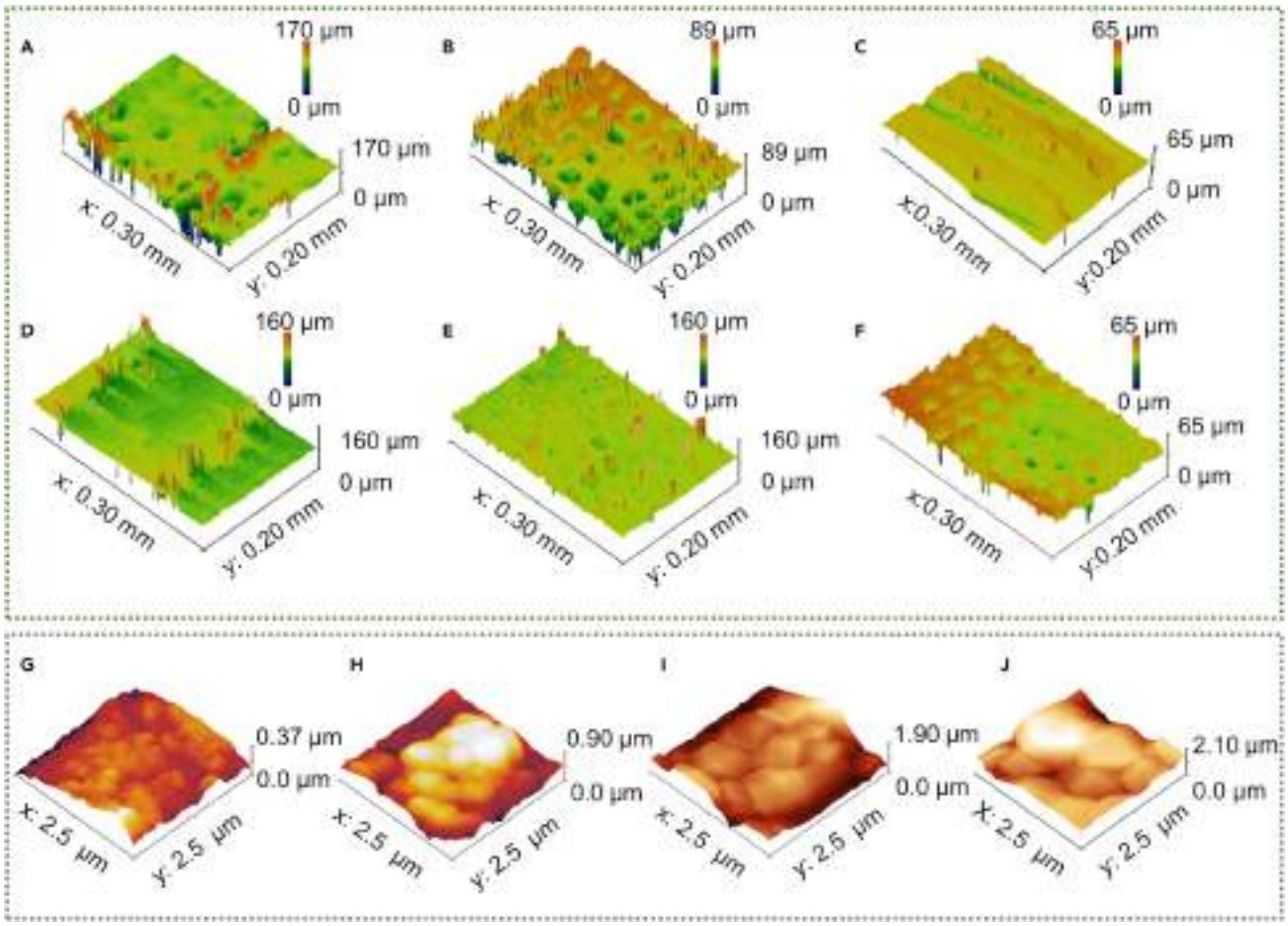

Figure 3. Surface roughness of native wood and functionalized wood samples

(A–F) 3D surface profiles obtained by optical profilometry for (A) cross-cut native balsa, (B) cross-cut native spruce, (C) tangential-cut native spruce veneer, (D) radial-cut native spruce, (E) PDMS@spruce(C), (F) 20-ZIF-8@spruce(C).

(G–J) AFM results for 1-(MeIm/Zn)@spruce(C) and ZIF-8@spruce(C) samples. The 2-MeIm/Zn^{2+} ratio is increased from 1 to 5, 10, 20, respectively.

(11.4 μm), native spruce(R) and native spruce(T) have much lower Ra values, respectively of 6.3 and 7.6 μm (Table S3). The higher Ra value of cross-cut wood samples may result from their highly porous structure. These different Ra parameters are representative of the inherent roughness of the wood surface, which originates from the specific arrangement of microscale cells. As shown in Figures 3E and S13 and Table S3, the wood surface roughness after coating with PDMS is significantly reduced at the microscale, consistent with SEM results. Modifying the wood scaffold with ZIF-8 reduced by a certain extent the overall microscale roughness (Figures 3F and S14 and Table S3), but at the same time increased the nanoscale surface roughness. This change of nanoscale roughness was investigated by atomic force microscopy (AFM), imaging on the early-wood's cell wall of cross-cut spruce with a scan size of 2.5 μm × 2.5 μm. As shown in Figures 3G–3J and Table S4, when the 2-MeIm/Zn^{2+} ratio increased from 5 to 20, the Ra of ZIF-8@wood increased gradually from 169.1 nm to 286.5 nm. When the 2-MeIm/Zn^{2+} ratio is 1, the Ra of 1-(MeIm/Zn)@spruce(C) has a lowest value of 37.1 nm. Modification with *in situ*-grown ZIF-8 can be a valid method to adjust the surface nano-roughness of triboelectric materials. In the following, we show that the modification of wood both with ZIF-8 and with PDMS plays an essential role in enhancing the electrical output of our FW-TENG by improving the surface roughness.

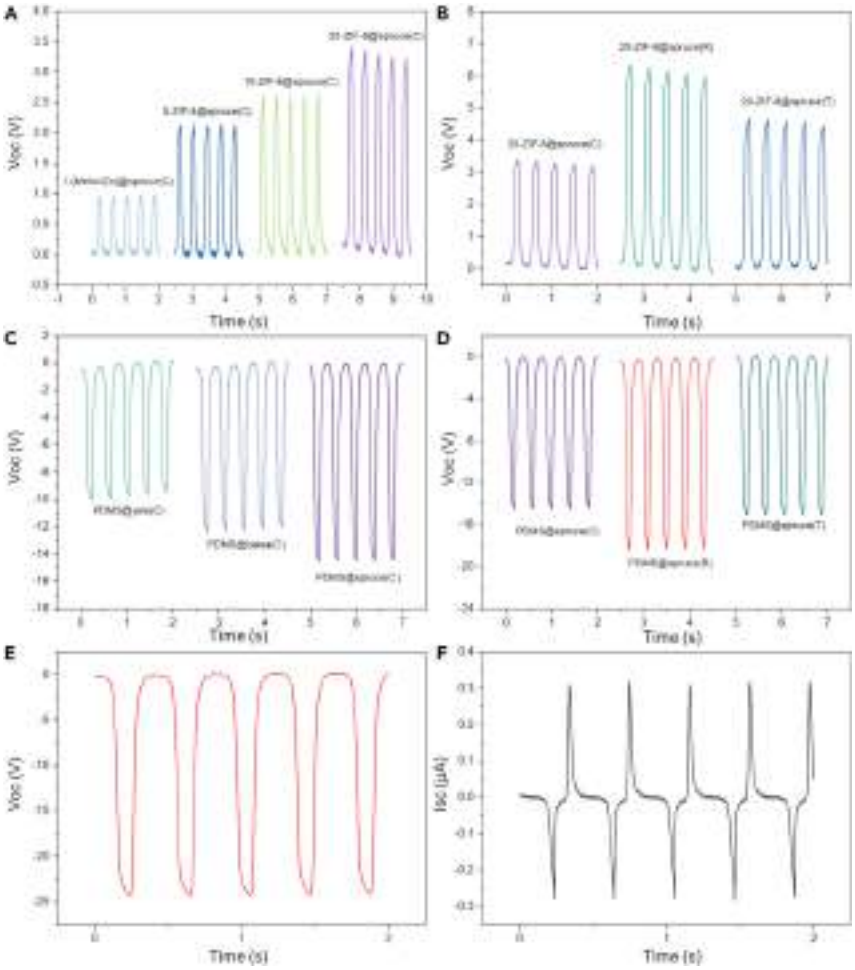

Figure 4. Effect of different parameters on the triboelectric performance of FW-TENG

(A–D) Effect of different parameters on the open-circuit voltage of functionalized wood TENGs. All samples are tested against radial-cut native wood (reference material). (A) ZIF-8@spruce(C) samples: effect of the 2-MeIm/Zn^{2+} ratio. In addition, the 1-(MeIm/Zn)@spruce(C), which does not form ZIF-8, shows lowest Voc. (B) ZIF-8@spruce: effect of cutting direction. A constant 2-MeIm/Zn^{2+} ratio of 20 is used. (C) PDMS@wood samples: effect of the wood species. (D) PDMS@wood samples: effect of cutting direction.

(E) Open-circuit voltage and (F) short-circuit current for an optimized FW-TENG made of 20-ZIF-8@spruce(R) and PDMS@spruce(R).

The triboelectric performance of native and functionalized wood samples was systematically evaluated with a Keithley 6514. The sample to be tested was paired with a piece of radial-cut native spruce as reference material to make a TENG with a simple vertical contact-separation design. The surface area was kept constant (2 cm × 3.5 cm), and the force applied was 50 N. As shown in Figures 4A and S15, the electrical output of ZIF-8@spruce(C) gradually increases for increasing 2-MeIm/Zn^{2+} ratios, reaching a maximum open-circuit voltage (Voc) of 3.2 V and short-circuit current (Isc) of 0.037 μA for a 2-MeIm/Zn^{2+} ratio of 20. This result may be attributed to the tribopositive nature of ZIF-8 and the gradual increase of nanoscale roughness observed, when the size of ZIF-8 nanocrystals grown onto wood is increased by using higher MeIm/Zn^{2+} ratios. To demonstrate the superior properties of *in situ* ZIF-8 growth compared with physical deposition, a 20-ZIF-8@spruce(C) sample was prepared by physical coating and its triboelectric performance was

evaluated. The open-circuit voltage was much lower (Voc = 1.1 V) compared with that of a sample prepared by chemical coating (Voc = 3.2 V). We attribute this decreased performance to the less homogeneous distribution of ZIF-8 nanoparticles and their reduced interaction with the wood scaffold (Figure S16). After selecting the most suitable 2-MeIm/Zn^{2+} ratio and composite preparation method, we investigated the effects associated with the wood scaffold, including the choice of wood species and cutting direction. Since balsa wood modified with ZIF-8 shrinks considerably, its electrical output has not been measured. Regarding the electrical output of ZIF-8@yew(C) samples, as shown in Figure S17, 20-ZIF-8@yew(C) tends to generate Voc and Isc values similar to those of 20-ZIF-8@spruce(C). However, yew is less available and more expensive compared with spruce, making spruce a better candidate for large-scale applications. For this reason, ZIF-8 was grown on radial- and tangential-cut spruce to investigate the influence of the cutting directions on the electrical performance of ZIF-8@spruce composites. As shown in Figures 4B and S18, 20-ZIF-8@spruce(R) and 20-ZIF-8@spruce(T) generated a higher electrical output than 20-ZIF-8@spruce(C). This result may be attributed to the highly porous structure of cross-cut wood scaffolds, with big, deep pores (tracheid lumina) that reduce the effective contact surface areas. The highest Voc and Isc values generated by 20-ZIF-8@spruce(R) are 6.0 V and 0.07 μA, respectively. A control experiment, in which two pieces of native radial-cut spruce were assembled into a TENG, was made to evaluate the impact of ZIF-8 modification on the electrical performance of wood. As shown in Figure S19, this native wood TENG generated ultra-low Voc and Isc under 50 N, respectively 0.3 V and 0.004 μA, resulting from poor polarizability of wood and the weak triboelectrification effect between two identical materials. It is clear from these results that the functionalization with ZIF-8 significantly increases the electron-donating ability of wood, incrementing the electrical output by about 20 times. Conversely, modification of wood with PDMS gave it a strong electron-accepting behavior. The three wood species (spruce, balsa, yew) were cross-cut and coated with PDMS, and assembled in a TENG against radial native spruce as reference material, all other parameters being the same as discussed for the ZIF-8@wood samples. As shown in Figures 4C and S20, PDMS@spruce(C) performs best while PDMS@yew(C) generates the lowest electrical output. These results may be attributed to the effect of surface roughness, as PDMS@yew(C) has a much smoother surface than PDMS@spruce(C). Spruce was then selected to further investigate the effect of cutting direction. Figures 4D and S21 show that radial-cut spruce wood coated with PDMS generates maximum Voc and Isc values of 18.5 V and 0.25 μA, respectively. These results indicate that coating PDMS on wood greatly increases the electron-accepting ability of wood, with an increment of the electrical output of over 60 times. The modification with ZIF-8 and PDMS enhances the tribopolarity of wood to opposite directions, allowing widening the spectrum of triboelectric behavior (Figure S22). As shown in Figures 4E and 4F, an optimized FW-TENG made with a pair of 20-ZIF-8@spruce(R) and PDMS@spruce(R) samples (each with dimensions 2 cm × 3.5 cm) could generate maximum Voc and Isc of 24.3 V and 0.32 μA, respectively, an output that is over 80 times higher than that of a native wood TENG. The transferred charge density of the FW-TENG is shown in Figure S23, with a peak value of 12 μC m^{-2}.

We wanted to improve the triboelectric properties of wood without losing its compelling merits as a building material, such as mechanical robustness and warm colors, even at the price of a lower electrical performance. For this reason, the thickness of wood used in our work is much higher compared with that of more conventional triboelectric materials.[42,43] This weakens the electrostatic induction effect, reducing the electrical output.

Decreasing the thickness is one possible approach to improve the performance of our FW-TENG.[42] Another possibility is to use a different configuration for the PDMS@wood, such as the one shown in Figure S24B, in which the copper foil electrode is placed directly between PDMS and wood. We evaluated the performance of an FW-TENG in this new configuration by pairing the new PDMS@spruce(R) with a 20-ZIF-8@spruce(R), all the other parameters being the same. The output was indeed higher, with a Voc of 80 V and an Isc of 1 μA (Figures S24C and S24D), but this is not the only difference. In this configuration, wood acts purely as a mechanical support for the soft PDMS film. The advantages brought by the use of wood as a microstructuring template, enhancing the surface roughness of PDMS at the micro- and nanoscale, could be kept only by using a highly compliant conductive material as the electrode, for example by substituting the copper foil with e.g., silver ink. By contrast, in our original configuration (Figure S24A), the microstructure of wood can always be used regardless of the nature of the electrode. Since this new configuration sacrifices some of the merits of wood and, to a certain degree, lacks useful insight for tuning the triboelectric properties of wood itself, in the present study we focused on the original configuration, knowing that more dedicated research will be needed to efficiently solve the trade-off dilemma between mechanical strength of wood and its triboelectric performance.

A long-term cyclic test was performed to evaluate the mechanical stability of the optimized FW-TENG under a constant force of 50 N. As shown in Figure S25, the output Voc was stable at approximately 24.3 V with minor fluctuations for up to 1,500 cycles, indicating good stability. The electricity produced by our FW-TENG could be used to power directly small electronic devices, or could be stored, e.g., in a capacitor, for later use. As shown in Figure 5A, commercial capacitors with three different capacities (0.1 μF, 0.47 μF, and 2.2 μF) were charged using the optimized FW-TENG. In 30 s, the 0.1 μF capacitor could reach 8.9 V, the 0.47 μF capacitor could reach 2.2 V, while the 2.2 μF capacitor could only reach 0.48 V. External resistors varying from 0.1 to 120 MΩ were connected to the FW-TENG to measure its actual power. As shown in Figure 5B, the voltage gradually increases when the resistance is increased, and eventually reaches a plateau. A maximum instantaneous power of 7.3 μW (corresponding to a power density of 10.4 mW m^{-2}) was obtained with an optimized load resistance of 80 MΩ. Scalability is a parameter of great importance to enable applications of TENGs in smart buildings. The scalability of our optimized FW-TENG was then demonstrated by increasing the size of the functionalized wood samples to 10 cm × 8 cm. These large-scale samples of PDMS@wood and ZIF-8@wood were prepared with the same protocols used for the small samples. As shown in Figures 5C and 5D, this large-scale FW-TENG can generate a Voc and Isc of 79.6 V and 0.94 μA under a force of 50 N, demonstrating its suitability for application in energy-generating floorings. Recent developments in wood- or cellulose-based TENGs are summarized in Table S5.[44,45] Previous efforts focused on coupling wood or cellulose with highly polarizable materials, such as PTFE, to maximize the electrical output. However, using expensive and non-biodegradable synthetic polymers makes large-scale applications (e.g., as building floorings) of such TENGs unsustainable from both the economic and environmental perspective. Our functionalized wood TENG shows an average electrical output, but has the advantage of reduced materials cost and environmental impact, and it may be of inspiration for future studies on tuning wood tribopolarity.

Mechanical strength is another important factor for materials to be used in building applications. Therefore, the optimized composites were characterized also by means of tensile tests (Figures 5E and 5F). The ultimate tensile strengths

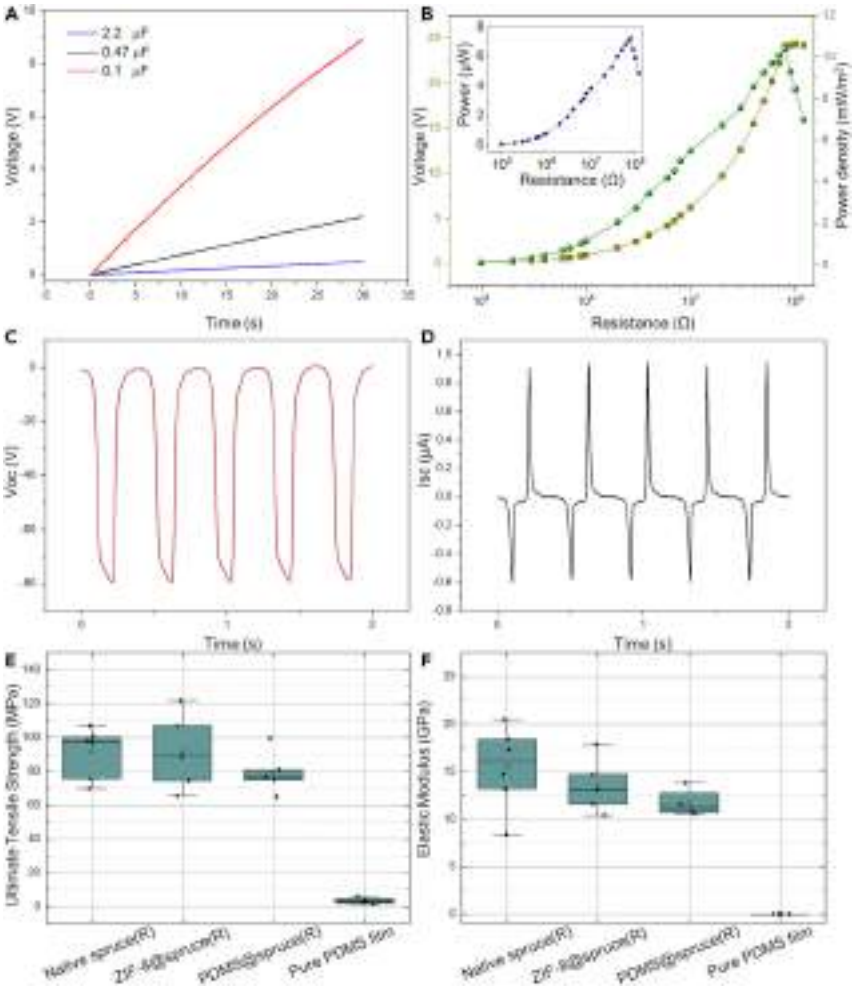

Figure 5. Power output and performance of normal- and large-scale FW-TENGs

(A)Voltage profile of capacitors (0.1 μF, 0.47 μF, 2.2 μF) when charged by the optimized FW-TENG.

(B) Electrical output performance of the optimized FW-TENG with an external loading resistance. Inset: power density.

(C and D) (C) Open-circuit voltage and (D) short-circuit current of the larger-scale optimized FW-TENG (10 cm × 8 cm) under a force of 50 N.

(E) Ultimate tensile strengths and (F) stiffness of native spruce(R) and ZIF-8@spruce(R), PDMS@spruce(R), and pure PDMS film.

of ZIF-8@spruce(R) and PDMS@spruce(R) were 91.4 ± 20.7 MPa and 79.5 ± 11.4 MPa, values comparable with that of native spruce(R) (91.4 ± 13.6 MPa). For comparison, pure PDMS films with the same shape and thickness were also tested. Their ultimate tensile strength is more than an order of magnitude lower (3.4 ± 1.7 MPa), making them unsuitable for building applications. Stiffness values (Figure 5F) of ZIF-8@spruce(R) and PDMS@spruce(R), respectively 13.5 GPa and 11.7 GPa, were also high, slightly lower compared with native spruce(R) (15.4 GPa). Without the support of a wood scaffold, the elastic modulus of pure PDMS films is only 2 MPa.

Moreover, the natural wood surface color is preserved both after the *in situ* growth of ZIF-8 and spin coating of PDMS, as can be seen in Figure S26 and by the small color change (ΔE^*) values listed in Table S6. This is especially important for indoor building applications, in which the warm colors of wood are highly appreciated.[46]

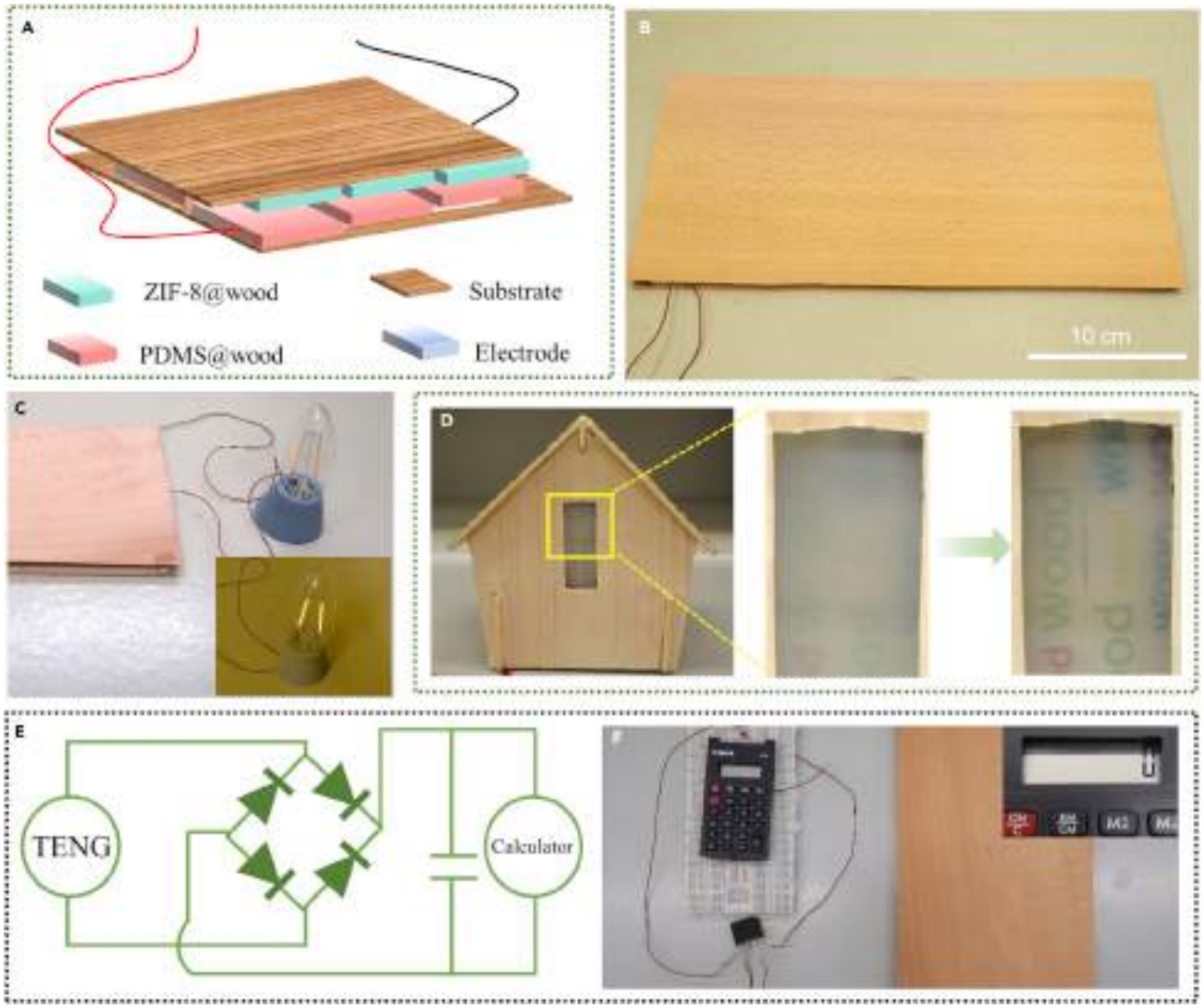

Figure 6. Practical smart home applications of our TENG

(A–D) (A) Schematic representation and (B) photograph of an optimized large FW-TENG (45 cm × 20 cm) made of six pairs of functionalized wood with opposite tribo-polarities, which was used to power (C) a household lamp (2 W, E14), (D) the smart window of a model wooden house, and (E and F) a calculator.

As schematically represented in Figure 6A, many large-scale optimized FW-TENGs can be assembled, connecting more elements in series or in parallel to maximize the electrical output allowing the powering of more energy-intensive devices. To further demonstrate the up-scaling potential of our FW-TENGs for integration in smart buildings, we fabricated a triboelectric wooden floor demonstrator made of six electrically connected optimized FW-TENGs (10 cm × 8 cm each). As shown in Figures 6B and S27, copper foils with a size of 30 cm × 16 cm were attached to the back of 20-ZIF-8@spruce(R) and PDMS@spruce(R) samples, respectively. Then, the copper foil on each side was covered with a larger native wood veneer (35 cm × 20 cm × 0.1 cm). Conductive wires were led out from the copper foils and directly connected to a household lamp (2 W, E14). As shown in Figure 6C and Video S1, the lamp could be readily switched on when the wood floor prototype was walked upon by a human adult. Figure 6D and Video S2 display the powering of an electrochromic window in a small model house. The window is initially opaque, and

becomes transparent when the FW-TENG is pressed by hand. As previously mentioned, the electricity produced could be stored in capacitors. Thus, a circuit connecting the FW-TENG model floor with a commercial full-wave bridge rectifier was designed to power a commercial calculator with the assistance of a 0.1-μF capacitor, as depicted in Figure 6E. In the beginning, the capacitor is empty. The demonstrator was repeatedly pressed for a few seconds, then the calculator could be connected to the capacitor to be powered (see Figure 6F and Video S3). These proof-of-concept applications demonstrate that applicability of large-scaled FW-TENGs in smart buildings.

DISCUSSION

We demonstrated that the otherwise negligible triboelectric behavior of native wood could be strongly enhanced by functionalization with ZIF-8 and PDMS, making it possible to fabricate self-powering floors with enhanced wood TENG for smart homes. Compared with native wood, ZIF-8@wood is 20 times more tribopositive, while PDMS@wood is about 60 times more tribonegative. These dramatic changes of tribopolarity are attributed to physical changes (surface morphology and an increase of contact surface area by the treatment) and chemical changes (caused by the introduction of efficient electron-accepting and electron-donating species). Two wood samples (20 × 35 × 1 mm^3), one functionalized with ZIF-8 and the other coated with PDMS, could generate a maximum open-circuit voltage of 24.3 V and a short-circuit current of 0.32 μA under a relatively small force of 50 N, which is 80 times higher than that generated by native wood. The output electricity could be increased by assembling six larger wood TENGs (100 × 80 × 1 mm^3), sufficient to drive both household LED (light-emitting diode) lamps and calculators. Furthermore, our wood TENG could power smart electrochromic windows to modulate sunlight transmittance, reducing the energy consumption for lighting. Both functionalization techniques, *in situ* growth of ZIF-8 and spin coating of PDMS, preserved to a great extent the compelling properties of wood (e.g., mechanical stability and warm colors), making the resulting materials suitable for high-end building applications. The efficient electrical output, the sustainability, and the scalability of radial-cut wood may contribute to the design of the next generation of sustainable power supplies in smart buildings.

EXPERIMENTAL PROCEDURES

Resource availability

Lead contact

Further information and requests for resources and materials should be directed to and will be fulfilled by the lead contact, Dr. Guido Panzarasa (guido.panzarasa@ifb.baug.ethz.ch)

Materials availability

This study did not generate any new unique materials.

Data and code availability

This study did not generate/analyze datasets/code.

Materials

Cross sections of native wood species, including Norway spruce (*Picea abies*), balsa (*Ochroma pyramidale*), and European yew (*Taxus baccata*) with the dimensions of 35 mm × 20 mm × 1 mm (radial × tangential × longitudinal, R × T × L) were cut by a laser cutter (Trotec, Speedy 300). Radial sections and tangential sections of native wood with the dimensions of 20 mm × 1 mm × 35 mm (R × T × L) and of

1 mm × 20 mm × 35 mm (R × T× L) were cut by saw, respectively. Zinc nitrate hexahydrate ($Zn(NO_3)_2 \cdot 6H_2O$, 98%), methanol (≥99.9%), and ethanol (≥99.8%) were purchased from Sigma-Aldrich. 2-Methylimidazole (2-MeIm, 97%) and sodium hydroxide (NaOH) were provided by Thermo Fisher GmbH. PDMS (Sylgard 184) prepolymer and curing agent were supplied by Dow Corning Co., Ltd. (Michigan, United States). All chemicals were used as received.

Synthesis of ZIF-8@wood

The preparation of ZIF-8@wood samples was adapted from a method reported by Tu et al.[19] Native wood samples were pretreated by immersion in a 15% w/v NaOH aqueous solution for 1 h. The wood samples were first washed with water and then immersed in an NaOH solution (pH = 9) until pH stabilized. These pretreated wood samples were submerged in a mixture of 0.002 mol of $Zn(NO_3)_2$, 20 g of methanol, and 3 g of deionized water for 2 h to ensure a sufficient ion exchange between Zn and Na ions. A mixture of 0.04 mol of 2-MeIm, 20 g of methanol, and 3 g of deionized water was subsequently added to the above solution. Stirring at room temperature for 24 h led to the ZIF-8@wood composite. The composite was then rinsed with methanol to remove the unreacted precursors (until the washing solution was transparent), followed by drying in the vacuum oven at 103°C for 24 h. The 2-MeIm/Zn^{2+} molar ratio in the precursor solution ranged from 1, 5, 10, to 20, and the corresponding names of the composites are 1-(MeIm/Zn)@spruce(C), 5-ZIF-8@wood, 10-ZIF-8@wood, and 20-ZIF-8@wood.

Fabrication of PDMS@Wood

The PDMS solution was prepared by mixing the Sylgard 184 elastomer with the curing agent in 10:1 proportion and stirring for 1 min. After that, the PDMS mixture was kept in a vacuum for 20 min to remove air bubbles. The as-prepared mixture of PDMS was coated on the wood by spin coating at 2000 rpm for 30 s, and eventually cured at 60°C for 2 h.

20-ZIF-8@spruce(C) prepared by physical coating

Solutions of $Zn(NO_3)_2 \cdot 6H_2O$ (0.002 mol) and 2-MeIm (0.04 mol) were prepared by dissolving each reactant in a mixture of 20 g of methanol and 3 g of deionized water. These two solutions were mixed together and stirred at room temperature for 24 h. After washing with methanol (3 × 60 cm^3), the 20-ZIF-8 particles were dispersed in 50 g of methanol to form a 20-ZIF-8 suspension. 20-ZIF-8@spruce(C) samples were obtained by immersing native spruce(C) into the as-prepared 20-ZIF-8 suspension for 1 min, followed by drying at 103°C under vacuum.

Device fabrication

A triboelectric wooden floor demonstrator was made of six pairs of optimized 20-ZIF-8@spruce(R) and PDMS@spruce(R) samples (10 cm × 8 cm each piece). Commercial copper foil (30 cm × 16 cm) was attached to the back of six 20-ZIF-8@spruce(R) (30 cm × 16 cm in total) and six PDMS@spruce(R) (30 cm × 16 cm in total) samples, respectively. Finally, the copper foil on each side was covered with a larger native wood veneer (35 cm × 20 cm × 0.1 cm). Conductive wires were led out from the copper foils and directly connected to the testing instrument or external electronic devices.

Characterization techniques

SEM

Wood samples were cut into small cubes of 5 mm × 5 mm × 1 mm. Then they were put into a vacuum oven at 103°C for 2 h for drying. Afterward, the wood samples

were coated with 10-nm Pt/Pd (80/20) film using a sputter coater (CCU-010, Safematic, Switzerland) to make the surface conductive. The structure of the samples was characterized by field emission SEM (FEI Quanta 200F).

AFM

AFM imaging was carried out using a NanoWizard 4 (JPK Instruments AG, Bruker Nano GmbH, Germany) at 20°C and 65% relative humidity climate room. The cross-cut wood samples were glued on a glass slide. Measurements were performed in alternating contact (AC) mode, using rectangular silicon cantilevers (NCHR-10, Nano World, Switzerland) with a resonant frequency of 320 kHz and a nominal spring constant of 42 N m^{-1}. A scan size of 2.5 μm × 2.5 μm and a resolution of 256 × 256 pixels was used. Imaging was performed at a gain range from 150.0 to 350.0, scanning rates of 0.5 Hz, and setpoint amplitudes of 65%–75% of the free oscillation amplitude. All images were plotted using the Gwyddion software (v 2.57).

Optical profilometry

3D images of W-TENG samples were acquired with a Sensofar Plu Neox optical profilometer (Seonsofar, Spain). The optical profiling instruments employed a 20× objective with a light beam and scanned under a resolution of 768 × 576 pixels. The scan size was 636.61 × 477.25 μm^2, and the Z scan was between 80 and 150 μm with a threshold of 0.2%. Data were plotted using Gwyddion software (v 2.57), in which a smaller size (300 μm × 200 μm) was selected.

FTIR

Thin wood samples were analyzed with an attenuated total reflectance Fourier-transform infrared (ATR-FTIR) spectrometer (Bruker Tensor 27) equipped with an ATR module over the scan range of 400–4000 cm^{-1} to see the composition of the chemical change of sample surface upon PDMS and ZIF-8 modification. Before using the baseline concave rubber-band correction method to do baseline correction, the spectra from five samples were averaged. Data were normalized in the OPUS software and plotted in OriginPro 9.6.

XRD

The crystal structure of ZIF-8@wood was studied by XRD (Panalytical X'Pert PRO MPD) using copper Kα radiation (λ = 1.5406 Å). Small cross-cut ZIF-8@spruce samples with a thickness of 1 mm, a length of 2 cm, and a width of 1 cm were used for the measurements. The diffraction data were conducted with an angular step size of 0.03° and a counting time of 1 s per step and recorded in the 2θ 5°–70° range.

ICP-OES

ICP-OES was conducted using a Horiba Ultra 2 instrument equipped with photomultiplier tube detection. The samples were digested in an MLS turboWave microwave by heating the material (ca. 10–15 mg) in 3 cm^3 of a 3:1 volumetric mixture of HNO_3 (Sigma-Aldrich, ≥65 wt %) and H_2O_2 (Sigma-Aldrich, 35 wt %) to 533 K for 50 min with a maximum power of 1,200 W and a loading pressure of 70 bar. The obtained clear solutions were filtered and diluted to 25 mL with ultrapure water prior to analysis. The mass percentage of ZIF-8 was calculated from the measured Zn content assuming an ideal stoichiometry for ZIF-8 ($C_8H_{10}N_4Zn$). The error was estimated as the standard deviation of three independent measurements.

Measurement of electrical output

A linear motor (PL01-28x500/420) was used to load the samples with a fixed force. At the same time, a loading cell was mounted on the rigid frame of the motor to monitor

the pressure applied to the samples. The electrical output was measured by a Keithley 6514, equipped with a MATLAB software.

Mechanical tensile testing

Tensile tests were conducted on a Zwick/Roell Z010 universal testing machine. The measurements were made with a 10-kN and a 1-kN load cell for the wood-based samples and the PDMS film (1-mm thickness), respectively. The samples were cut into dog-bone shape according to ISO 527-3[47] specimen type 5 parallel to the fiber direction. Additionally, spruce tags were glued to the grip section of the samples as reinforcement. The testing speed was 0.4 mm/min. The E-modulus was calculated by the slope of a linear regression in the range between 10% and 40% of the maximal force.

Measurement of color changes

Changes in color of wood surface were measured with a Minolta spectrophotometer (CR200, Japan) using the CIE L*a*b* system based on the ISO 7724 standard test method.[48] The average values of the color parameters were obtained by measuring 10 different positions for each sample. In the CIE L*a*b* system, L represents lightness, and a and b represent chromaticity parameter. The overall color change (ΔE^*) was calculated according to the following equation (Equation 1):

$$\Delta E^* = \sqrt{\Delta a^2 + \Delta b^2 + \Delta L^2} \quad \text{(Equation 1)}$$

where ΔL, Δa, and Δb represent the changes in L, a, and b between the values of native wood and plasma-treated wood, respectively. A lower ΔE^* value corresponds to a lower color change.

SUPPLEMENTAL INFORMATION

Supplemental information can be found online at https://doi.org/10.1016/j.matt.2021.07.022.

ACKNOWLEDGMENTS

The project was conducted with the support by the SNF project Hierarchical Cellulose Scaffolds for Structural and Functional Gradient Materials (200021_184821/1). The authors thank Thomas Schnider for the wood sample preparation and the technical support. The authors thank Nicolas Bain for access to the spin-coater. K.T. thanks financial support from the China Scholarship Council (CSC) (201703270028).

AUTHOR CONTRIBUTIONS

J.S. and K.T contributed equally to this work. J.S., K.T., and G.P. conceived the study. J.S., K.T., S.B., S.M.K., Y.D., and S.S. performed experiments and analyzed data. S.M.K., S.N.R., H.G., C.W., T.K., J.P.R., and I.B. verified the experimental design and data analysis, and gave theoretical support. J.S., K.T., and G.P. co-wrote the manuscript. All authors discussed the results and commented on the manuscript.

DECLARATION OF INTERESTS

The authors declare no competing interests.

Received: May 4, 2021
Revised: June 29, 2021
Accepted: July 30, 2021
Published: September 1, 2021

REFERENCES

1. Bell, L.E. (2008). Cooling, heating, generating power, and recovering waste heat with thermoelectric systems. Science *321*, 1457–1461.

2. Fan, F.R., Tian, Z.Q., and Wang, Z.L. (2012). Flexible triboelectric generator! Nano Energy *1*, 328–334.

3. He, C., Zhu, W.J., Chen, B.D., Xu, L., Jiang, T., Han, C.B., Gu, G.Q., Li, D.C., and Wang, Z.L. (2017). Smart floor with integrated triboelectric nanogenerator as energy harvester and motion sensor. ACS Appl. Mater. Interfaces *9*, 26126–26133.

4. Song, Y., Wang, H.B., Cheng, X.L., Li, G.K., Chen, X.X., Chen, H.T., Miao, L.M., Zhang, X.S., and Zhang, H.X. (2019). High-efficiency self-charging smart bracelet for portable electronics. Nano Energy *55*, 29–36.

5. Parida, K., Xiong, J.Q., Zhou, X.R., and Lee, P.S. (2019). Progress on triboelectric nanogenerator with stretchability, self-healability and bio-compatibility. Nano Energy *59*, 237–257.

6. Hao, S.F., Jiao, J.Y., Chen, Y.D., Wang, Z.L., and Cao, X. (2020). Natural wood-based triboelectric nanogenerator as self-powered sensing for smart homes and floors. Nano Energy *75*, 104957.

7. Chandrasekhar, A., Vivekananthan, V., Khandelwal, G., Kim, W.J., and Kim, S.J. (2020). Green energy from working surfaces: a contact electrification-enabled data theft protection and monitoring smart table. Mater. Today Energy *18*, 100544.

8. Kim, I., Jeon, H., Kim, D., You, J., and Kim, D. (2018). All-in-one cellulose based triboelectric nanogenerator for electronic paper using simple filtration process. Nano Energy *53*, 975–981.

9. Zhang, L., Liao, Y., Wang, Y.C., Zhang, S.V., Yang, W.Q., Pan, X.J., and Wang, Z.L. (2020). Cellulose II aerogel-based triboelectric nanogenerator. Adv. Funct. Mater. *30*, 2001763.

10. Sun, J.G., Yang, T.N., Kuo, I.S., Wu, J.M., Wang, C.Y., and Chen, L.J. (2017). A leaf-molded transparent triboelectric nanogenerator for smart multifunctional applications. Nano Energy *32*, 180–186.

11. Sun, J.G., Yang, T.N., Wang, C.Y., and Chen, L.J. (2018). A flexible transparent one-structure tribo-piezo-pyroelectric hybrid energy generator based on bio-inspired silver nanowires network for biomechanical energy harvesting and physiological monitoring. Nano Energy *48*, 383–390.

12. Sun, J.G., Guo, H.Y., Ribera, J., Wu, C.S., Tu, K.K., Binelli, M., Panzarasa, G., Schwarze, F.W.M.R., Wang, Z.L., and Burgert, I. (2020). Sustainable and biodegradable wood sponge piezoelectric nanogenerator for sensing and energy harvesting applications. ACS Nano *14*, 14665–14674.

13. Diaz, A.F., and Felix-Navarro, R.M. (2004). A semi-quantitative tribo-electric series for polymeric materials: the influence of chemical structure and properties. J. Electrostat. *62*, 277–290.

14. Muthu, M., Pandey, R., Wang, X.Z., Chandrasekhar, A., Palani, I.A., and Singh, V. (2020). Enhancement of triboelectric nanogenerator output performance by laser 3D-surface pattern method for energy harvesting application. Nano Energy *78*, 105205.

15. Seung, W., Gupta, M.K., Lee, K.Y., Shin, K.S., Lee, J.H., Kim, T.Y., Kim, S., Lin, J., Kim, J.H., and Kim, S.W. (2015). Nanopatterned textile-based wearable triboelectric nanogenerator. ACS Nano *9*, 3501–3509.

16. Yun, B.K., Kim, J.W., Kim, H.S., Jung, K.W., Yi, Y., Jeong, M.S., Ko, J.H., and Jung, J.H. (2015). Base-treated polydimethylsiloxane surfaces as enhanced triboelectric nanogenerators. Nano Energy *15*, 523–529.

17. Luo, J.J., Wang, Z.M., Xu, L., Wang, A.C., Han, K., Jiang, T., Lai, Q.S., Bai, Y., Tang, W., Fan, F.R., and Wang, Z.L. (2019). Flexible and durable wood-based triboelectric nanogenerators for self-powered sensing in athletic big data analytics. Nat. Commun. *10*, 5147.

18. Khandelwal, G., Chandrasekhar, A., Maria Joseph Raj, N.P., and Kim, S.J. (2019). Metal-organic framework: a novel material for triboelectric nanogenerator-based self-powered sensors and systems. Adv. Energy Mater. *9*, 1803581.

19. Tu, K.K., Puertolas, B., Adobes-Vidal, M., Wang, Y.R., Sun, J.G., Traber, J., Burgert, I., Perez-Ramirez, J., and Keplinger, T. (2020). Green synthesis of hierarchical metal-organic framework/wood functional composites with superior mechanical properties. Adv. Sci. *7*, 1902897.

20. Khandelwal, G., Maria Joseph Raj, N.P., and Kim, S.J. (2020). Zeolitic imidazole framework: metal-organic framework subfamily members for triboelectric nanogenerator. Adv. Funct. Mater. *30*, 1910162.

21. Denny, M.S., Moreton, J.C., Benz, L., and Cohen, S.M. (2016). Metal-organic frameworks for membrane-based separations. Nat. Rev. Mater. *1*, 1–17.

22. Wang, Z.L., Chen, J., and Lin, L. (2015). Progress in triboelectric nanogenerators as a new energy technology and self-powered sensors. Energ. Environ. Sci. *8*, 2250–2282.

23. Li, G.Z., Wang, G.G., Ye, D.M., Zhang, X.W., Lin, Z.Q., Zhou, H.L., Li, F., Wang, B.L., and Han, J.C. (2019). High-performance transparent and flexible triboelectric nanogenerators based on PDMS-PTFE composite films. Adv. Electron. Mater. *5*, 1800846.

24. Tantraviwat, D., Buarin, P., Suntalelat, S., Sripumkhai, W., Pattamang, P., Rujijanagul, G., and Inceesungvorn, B. (2020). Highly dispersed porous polydimethylsiloxane for boosting power-generating performance of triboelectric nanogenerators. Nano Energy *67*, 104214.

25. Yang, X.H., Zhu, G., Wang, S.H., Zhang, R., Lin, L., Wu, W.Z., and Wang, Z.L. (2012). A self-powered electrochromic device driven by a nanogenerator. Energ. Environ. Sci. *5*, 9462–9466.

26. Qiu, W.Z., Feng, Y.G., Luo, N., Chen, S.G., and Wang, D.A. (2020). Sandwich-like sound-driven triboelectric nanogenerator for energy harvesting and electrochromic based on Cu foam. Nano Energy *70*, 104543.

27. Yeh, M.H., Lin, L., Yang, P.K., and Wang, Z.L. (2015). Motion-driven electrochromic reactions for self-powered smart window system. ACS Nano *9*, 4757–4765.

28. Yang, Y., Zhang, H.L., Lin, Z.H., Zhou, Y.S., Jing, Q.S., Su, Y.J., Yang, J., Chen, J., Hu, C.G., and Wang, Z.L. (2013). Human skin based triboelectric nanogenerators for harvesting biomechanical energy and as self-powered active tactile sensor system. ACS Nano *7*, 9213–9222.

29. Li, S.Y., Fan, Y., Chen, H.Q., Nie, J.H., Liang, Y.X., Tao, X.L., Zhang, J., Chen, X.Y., Fu, E.G., and Wang, Z.L. (2020). Manipulating the triboelectric surface charge density of polymers by low-energy helium ion irradiation/implantation. Energ. Environ. Sci. *13*, 896–907.

30. Wang, Z.L. (2017). On Maxwell's displacement current for energy and sensors: the origin of nanogenerators. Mater. Today *20*, 74–82.

31. Wang, Z.L. (2020). On the first principle theory of nanogenerators from Maxwell's equations. Nano Energy *68*, 104272.

32. Zhang, H., Yao, L.J., Quan, L.W., and Zheng, X.L. (2020). Theories for triboelectric nanogenerators: a comprehensive review. Nanotechnol. Rev. *9*, 610–625.

33. Keunecke, D., Eder, M., Burgert, I., and Niemz, P. (2008). Micromechanical properties of common yew (*Taxus baccata*) and Norway spruce (*Picea abies*) transition wood fibers subjected to longitudinal tension. J. Wood Sci. *54*, 420–422.

34. Johnson, L.M., Gao, L., Shields, C.W., Smith, M., Efimenko, K., Cushing, K., Genzer, J., and Lopez, G.P. (2013). Elastomeric microparticles for acoustic mediated bioseparations. J. Nanobiotechnol. *11*, 1–8.

35. Lee, S., Lee, Y., Kim, D., Yang, Y., Lin, L., Lin, Z.H., Hwang, W., and Wang, Z.L. (2013). Triboelectric nanogenerator for harvesting pendulum oscillation energy. Nano Energy *2*, 1113–1120.

36. Park, S.J., Seol, M.L., Jeon, S.B., Kim, D., Lee, D., and Choi, Y.K. (2015). Surface engineering of triboelectric nanogenerator with an electrodeposited gold nanoflower structure. Sci. Rep. *5*, 13866.

37. Persson, B.N.J. (2006). Contact mechanics for randomly rough surfaces. Surf. Sci. Rep. *61*, 201–227.

38. Yang, W.X., Wang, X.L., Li, H.Q., Wu, J., Hu, Y.Q., Li, Z.H., and Liu, H. (2019). Fundamental research on the effective contact area of micro-/nano-textured surface in triboelectric nanogenerator. Nano Energy *57*, 41–47.

39. Dudem, B., Ko, Y.H., Leem, J.W., Lee, S.H., and Yu, J.S. (2015). Highly transparent and flexible triboelectric nanogenerators with

subwavelength-architectured polydimethylsiloxane by a nanoporous anodic aluminum oxide template. ACS Appl. Mater. Interfaces *7*, 20520–20529.

40. Su, Z.M., Han, M.D., Cheng, X.L., Chen, H.T., Chen, X.X., and Zhang, H.X. (2016). Asymmetrical triboelectric nanogenerator with controllable direct electrostatic discharge. Adv. Funct. Mater. *26*, 5524–5533.

41. Zhou, T., Zhang, L.M., Xue, F., Tang, W., Zhang, C., and Wang, Z.L. (2016). Multilayered electret films based triboelectric nanogenerator. Nano Res. *9*, 1442–1451.

42. Kang, X.F., Pan, C.X., Chen, Y.H., and Pu, X. (2020). Boosting performances of triboelectric nanogenerators by optimizing dielectric properties and thickness of electrification layer. Rsc Adv. *10*, 17752–17759.

43. Fan, F.R., Luo, J.J., Tang, W., Li, C.Y., Zhang, C.P., Tian, Z.Q., and Wang, Z.L. (2014). Highly transparent and flexible triboelectric nanogenerators: performance improvements and fundamental mechanisms. J. Mater. Chem. A *2*, 13219–13225.

44. Zheng, Q.F., Fang, L.M., Guo, H.Q., Yang, K.F., Cai, Z.Y., Meador, M.A.B., and Gong, S.Q. (2018). Highly porous polymer aerogel film-based triboelectric nanogenerators. Adv. Funct. Mater. *28*, 1706365.

45. Srither, S.R., Rao, D.S.S., and Prasad, S.K. (2018). Triboelectric nanogenerator based on biocompatible and easily available polymer films. Chemistryselect *3*, 5055–5061.

46. Rice, J., Kozak, R.A., Meitner, M.J., and Cohen, D.H. (2006). Appearance wood products and psychological well-being. Wood Fiber Sci. *38*, 644–659.

47. Zelazinski, T., Ekielski, A., Tulska, E., Vladut, V., and Durczak, K. (2019). Wood dust application for improvement of selected properties of thermoplastic starch. INMATEH-Agric. Eng. *58*, 37–44.

48. Tu, K.K., Wang, X.Q., Kong, L.Z., Chang, H.J., and Liu, J.L. (2016). Fabrication of robust, damage-tolerant superhydrophobic coatings on naturally micro-grooved wood surfaces. Rsc Adv. *6*, 701–707.